Mapping soil deformation around plant roots using *in vivo* 4D X-ray computed tomography and digital volume correlation

Keyes, S.D.[1,4], Gillard, F.[1], Soper, N.[2], Mavrogordato, M.N.[3], Sinclair, I,[3,4]., Roose, T.[1,4]*

1 – Bio-engineering Science Research Group, Faculty of Engineering and the Environment, University of Southampton, UK.

2 – Optoelectronics Research Centre, University of Southampton.

3 – μVIS Centre for Computed Tomography, University of Southampton.

4 – Crop Systems Engineering, Institute for Life Sciences, University of Southampton.

Keywords

Digital Volume Correlation, Soil, Granular Media, Plant Roots, Computational Biology, Computed Tomography, Biomechanics, X-ray Computed Tomography

Word Count: *3481*

Notation

DVC – Digital Volume Correlation

DIC – Digital Image Correlation

XCT – X-ray Computed Tomography

*Corresponding author: Building 5, Highfield Campus, University of Southampton, Southampton, SO17 1BJ, UK. S.D.Keyes@soton.ac.uk

Abstract (250)

The mechanical impedance of soils inhibits the growth of plant roots, often being the most significant physical limitation to root system development. Non-invasive imaging techniques have recently been used to investigate the development of root system architecture over time, but the relationship with soil deformation is usually neglected. Correlative mapping approaches parameterised using 2D and 3D image data have recently gained prominence for quantifying physical deformation in composite materials including fibre-reinforced polymers and trabecular bone. Digital Image Correlation (DIC) and Digital Volume Correlation (DVC) are computational techniques which use the inherent material texture of surfaces and volumes, captured using imaging techniques, to map full-field deformation components in samples during physical loading.

Here we develop an experimental assay and methodology for four-dimensional, *in vivo* X-ray Computed Tomography (XCT) and apply a Digital Volume Correlation (DVC) approach to the data to quantify deformation. The method is validated for a field-derived soil under conditions of uniaxial compression, and a calibration study is used to quantify thresholds of displacement and strain measurement. The validated and calibrated approach is then demonstrated for an *in vivo* test case in which an extending maize root in field-derived soil was imaged hourly using XCT over a growth period of 19 h. This allowed full-field soil deformation data and 3D root tip dynamics to be quantified in parallel for the first time.

This method paves the way for comparative studies of contrasting soils and plant genotypes, improving our understanding of the fundamental mechanical processes which influence root system development.

1. Introduction

Under limited water and/or nutrient availability, the development of an extensive root system is a key determinant of crop yield (Bengough et al., 2011). To penetrate soil, an individual root must either follow the path of an existing pore network (White and Kirkegaard, 2010), or displace soil material by a combination of rigid-body movement, shear and compression (Bengough et al., 2011). The study of these mechanisms has been hampered by the structural and chemical heterogeneity of soils (Young and Crawford, 2004), the sensitivity of soil mechanical properties to water status (Barré and Hallett, 2009; Whalley et al., 2005), and the inherent opacity of soil to visible light (Pierret et al., 2003).

X-ray Computed Tomography (XCT) is an established method for *in vivo* imaging of roots in soil (Gregory et al., 2003; Jenneson et al., 2003; Perret et al., 2007; Tracy et al., 2012). Recently, repeated 3D imaging over time (4D CT) has allowed the influence of bulk soil compaction on root system architecture to be quantified (Tracy et al., 2012). However, little is known at a fundamental level about the interplay of root growth phenomena and soil deformation. This is problematic since improved understanding and modelling of plant/soil systems will require dynamic morphology to be considered (Peth et al., 2010).

Digital correlation techniques are a promising tool for investigating deformation mechanics of porous media. By employing cross-correlation between grey-level values in reference and deformed images, full field components of material deformation can be computed. Vollsnes et al. (2010) have demonstrated two-dimensional digital image correlation (DIC) to map sand displacements around *Zea mays* roots in a rhizobox system. Others have combined XCT and digital volume correlation (DVC) to investigate sand and soil deformations under mechanical and hydraulic stresses (Hall et al., 2010; Peth et al., 2010; Schlüter et al., 2016). The latter approach offers substantial advantages over DIC. In 2D systems, deformation at the imaging plane is influenced by friction, shear and local compaction at the transparent interface, and quantification is limited to in-plane directions. Being a 3D method, XCT requires no transparent interface, and root tip positions do not need to be inferred from the deformation field (Vollsnes et al., 2010).

In this study, we combine XCT and DVC to map full-field soil displacements around an unconstrained plant root grown in field-derived soil for the very first time. The approach allows the root motion and soil deformation to be uncoupled and considered in parallel. Calibration studies are used to benchmark the accuracy of the method.

2. Materials and Methods

2.1. Soil preparation

A sandy loam (Eutric Cambisol) was collected from the surface Ah horizon of a plot at Abergwyngregyn, North Wales (53°14'N, 4°01'W). Following sieving to <5 mm to remove stones, autoclaving and air drying at 23 ± 1°C for 2 days, soil was sieved between bounds of 1680 μm and 1000 μm, producing a well-aggregated, textured growth medium. The resulting medium contained 52.7% sand, 32.8% silt and 14.5% clay. This soil was used in all subsequent experiments.

2.1. Plant material

Seeds of a maize cultivar (*Zea mays L. cv. Lark*) were germinated between sheets of damp Millipore filer paper at $21 \pm 2°\mathrm{C}$ for 48 h, at which point the mean length of primary roots was 4 mm.

2.2. Root growth chambers

Polypropylene centrifuge tubes of diameter 30 mm and height 115 mm were packed with soil to a bulk density of 1.09 $g \times cm^{-3}$. The soil was hydrated to field capacity (25.1% b.v.) and equilibrated for 3 days. ABS polymer seed cups were fabricated (UP! Printer, PP3DP, China) and affixed to the top of each tube (Figure 1). A 2.5 mm aperture allowed ingress of a single root to the soil chamber. A seed was inserted into each cup with the seminal root directed into the aperture, and the cup packed with quartz sand (<2 mm) to a depth of 30 mm to stabilise the seed. An unplanted control was also prepared. The microcosms were transferred to a controlled growth environment (Fitotron SGR, Weiss-Gallenkamp, Loughborough, UK) for 48 h of post-germination growth. Growth conditions were $23 \pm 1°\mathrm{C}$ and 60 % humidity for 16 h (day) and $18 \pm 1°\mathrm{C}$ and 55 % humidity for 8 h (night), both ramped over 30 minutes.

2.3. Tomographic Imaging

A rapid acquisition protocol was devised, using a Nikon HMX 225 ST micro-focus XCT scanner. Binning was applied, in which the signal from a 2x2 patch of adjacent detector elements is averaged together to form a larger 'virtual' detector element with enhanced counting statistics at a given X-ray flux and exposure. The optimal projection count (1571) was set according to $p \approx \pi \left(\frac{n}{2}\right)$, where p is the projection number and n is the number of elements across the detector. Energy was minimised to maximise the contrast to noise (CNR), with a tube voltage of 65 kV providing acceptable transmission at an exposure of 67 ms. The full parameters, giving an imaging time of 7 min per volume, are shown in Table 1. Volumes were reconstructed via a filtered back projection algorithm (CT Pro, Nikon Metrology, Tring, UK), normalised, rescaled and down-sampled to an 8-bit range. All samples were imaged under dark conditions at a temperature of 22 ±1°C.

2.4. DVC analysis

Digital Volume Correlation was applied to sequential volume pairs (a reference and deformed volume) using DaVis 8.2.2 software (LaVision, Goettingen, Germany), implementing a Fast Fourier Transform (FFT) approach to estimate local displacements. Within the reference dataset (S_n), each of $\boldsymbol{i}$ sub-volumes ($S_{n,i}$) can be represented by the grey-level function $f_i(x, y, z)$, and the corresponding deformed state ($S_{n+1,i}$) by the function $g_i(x + i, y + j, z + k)$, where (i, j, k) are the displacements mapping $S_{n,i}$ to $S_{n+1,i}$. Continuity of grey-levels is assumed, such that:

$$f_i(x, y, z) = g_i(x + i, y + j, z + k). \tag{1}$$

The objective is to find the vector $\vec{\boldsymbol{d}}_{i,n,x,y,z}$ mapping $S_{n,i}$ to $S_{n+1,i}$. Because the assumption in Equation 1 is deleteriously affected by noise and artifacts arising from data acquisition and reconstruction (Hall et al., 2010), confidence in each result must be verified by computing a correlation coefficient (see below).

Technical details of the correlation algorithm used to find the displacement vector of each sub-volume ($\vec{\boldsymbol{d}}_{i,n,x,y,z}$) are shown in Figure 2. A multi-pass approach was used to iteratively improve the accuracy, with the position of ($S_{n+1,i,search}$) being displaced by $-\vec{\boldsymbol{d}}_{i,x,y,z}$ after each pass, and the displacement re-computed. To reduce computational load, a large sub-volume edge length (l) was set initially, being made progressively smaller at each iteration . For a more in-depth technical discussion of DVC methods, the reader is referred to (Bay, 2008)

2.4.1. Quantification of systematic DVC error resulting from imaging artifacts

Because correlation depends on local grey-level information, results are sensitive to the ratio between the sub-volume edge length (l_s) and the characteristic feature size (l_f) (Liu and Morgan, 2007). If $l_s \leq l_f$, the grey-level distributions within each subvolume can be too homogenous to permit correlation, particularly if photon scattering, drift in detector output, and mechanical pertubations in the scanner mean noise and artifacts are prevalent (Gillard et al., 2014). Unfortunately, image quality parameters are deleteriously influenced by the rapid acquisition strategies required to image dynamic systems. Measurement precision can generally be improved by using larger sub-volumes, but at the cost of spatial resolution (White et al., 2003)

The optimal trade-off between sub-volume size and measurement precision is determined by correlating un-deformed pairs of control scans over a range of l_f (Gillard et al., 2014). One pair is generated at an identical sample location (Static 1 and Static 2); and one incorporates a rigid-body translation of 5 pixel edge-lengths between scans (Static 2 and Rigid 1). The reconstructed volume of Rigid 1 is translated to align with Static 2. In the ideal case, deformation for the two correlated pairs is zero everywhere due to the identical demand position, scan parameters and absence of external loading. The offset from zero and standard deviation in each deformation component thus represents the systematic error and noise in results respectively.

A randomly selected sample without roots was used for this noise study. Imaging was carried out using the XCT protocol described above, and the FFT algorithm in DaVis applied for correlation using edge lengths of 32, 52, 76, 104, 152, and 208 voxels.

2.4.2. Assessment of deformation mapping under uni-axial compression

If the sub-volume size is small relative to the magnitude of local displacements, the textural region enclosed by the reference sub-volume ($S_{n,i}$) may be entirely absent from the corresponding search window in the deformed volume ($S_{n+1,i,search}$). Furthermore, if deformation behaviour is complex (e.g. as a result of matrix collapse during loading), correlation between $S_{n,i}$ and $S_{n+1,i}$ can be poor (Gillard et al., 2014). Because a noise study alone cannot determine whether the sub-volume size is suitable given the magnitude of inter-scan deformation, a study was carried out to validate displacements in soil under conditions of simplified uniaxial compression.

A uniaxial compression rig was fabricated allowing a gauge volume of soil, of diameter 20.35 mm, to be compressed *in situ* within the XCT scanner (Figure S3-a). The soil was imaged four times, incorporating an upper platen displacement of 800 μm (compressive) between each scan, equivalent to the maximum extension of the root tip between scans. The three image pairs were correlated as above, using sub-volume edge lengths of 76, 104, 152 and 208 voxels. Displacements were neglected if the sub-volume incorporated the chamber wall, had a displacement magnitude below the threshold determined by the noise study, and/or returned a correlation coefficient of <0.9. In the literature the correlation coefficient is often left unstated, but a strict threshold was applied in this case to provide high confidence in the results (Gillard et al., 2014).

2.5. Plant growth case study

Rapid imaging of 5 samples was used to find a model sample with a largely vertical root growth orientation, thus avoiding root/wall interaction. This single sample was imaged for 20 h at an imaging frequency of 1 scan.h^{-1} using the protocol above.

2.6. Extraction of root data

The root morphology at each step was determined manually using FIJI (Schindelin et al., 2012) and a graphical input tablet (Cintiq 22HD, Wacom Co. Ltd., Saitama, Japan). Classified root cross-sections at ~20 voxel spacing were interpolated to form continuous volumes (Doube et al., 2010). These were meshed using ScanIP (Simpleware Ltd., Exeter, UK), smoothed in Meshlab (Cignoni et al., 2008) and exported as STL files for visualisation in Paraview (Ahrens et al., 2005). For each of the n scans, a vector ($\vec{v}_n$) linking the root tip position with that of the previous scan were recorded, and used to compute the angular rate of change in direction,

$$\Delta\theta\ (rad.h^{-1}) = \mathrm{atan}(\|\vec{v}_n \times \vec{v}_{n-1}\|, \vec{v}_n \cdot \vec{v}_{n-1}). \quad (1)$$

2.7. Qualitative deformation validation using deformation projections

To qualitatively assess matrix deformation for comparison with the DVC results, a difference volume ($V_{d,n}$) was computed for each image pair:

$$V_{d,n} = |V_n - V_{n+1}|, \quad (2)$$

where V_n is the reference volume, and V_{n+1} is the deformed volume. Each difference volume was averaged along x and y axes to generate 2D projections.

2.8. DVC analysis of soil deformation at the root tip

Sequential growth scans were correlated as described previously generating a 3D array for each displacement component (u_{xx}, u_{yy} and u_{zz}), and a corresponding array of correlation coefficients. Results for which the correlation coefficient was <0.9 were neglected, as were results below the significance threshold.

Strain components (ε_{ij}) were computed from the gradient of the displacement field using a centred finite difference scheme in MATLAB.

To compare the relative orientations of root growth and soil displacement, a magnitude-weighted mean of the angle between soil displacement vectors and the root growth vector was computed for each of the n growth steps, given by,

$$\varphi_n = \frac{\sum_{i=1}^{k} \mathrm{atan}(\|\vec{v}_n \times \vec{\boldsymbol{d}}_{i,n,x,y,z}\|, \vec{v}_n \cdot \vec{\boldsymbol{d}}_{i,n,x,y,z}) \cdot |\vec{\boldsymbol{d}}_{i,n,x,y,z}|}{k}, \quad (4)$$

where $\vec{\boldsymbol{d}}_{i,n,x,y,z}$ is the soil displacement vector for each of the k sub-volumes and the vector $\vec{v}_n$ is the root tip growth during step n. This value provides a measure of whether the root primarily displaces soil by driving it ahead of the root tip ($\varphi_n \to 0$), or whether soil is predominantly compressed out radially ($\varphi_n \to \frac{\pi}{2}$).

3. Results

3.1. Quantification of systematic DVC error resulting from imaging artifacts

The mean values of volumetric strain, shear and correlation coefficient converged by $l_s = 104$, and though the systemic error was such that displacement did not tend to zero, the values at $l_s = 104$ were lower than for larger l_s (Figure 4) Given that the degree of noise across all metrics had also converged by 104 voxels, this value was chosen for the plant study. The effective particle radius of ~45 voxels accords to the general rule for granular media that $l_s \sim 3 \times l_f$ (Peth et al., 2010). The significance thresholds were 0.395×10^{-3} mm for displacement and 0.315×10^{-5} for volumetric strain.

3.2. Validation of quantification under conditions of uni-axial compression

Figure S3-b shows plots of mean displacement components and volumetric strain with respect to z location for a single load step. The displacement component in the compression direction varied linearly with respect to distance from the upper platen; the expected behaviour for an ideal elastic material under compression. The maximum value was slightly lower than the upper platen displacement, and the minimum value slightly higher than zero, an artifact of the volume averaging inherent to the DVC method.

By calculating the normal strains for each sub-volume ($\varepsilon_{ij} = \frac{1}{2}(\frac{\partial u_i}{\partial x_j} + \frac{\partial u_j}{\partial x_i})$) from the gradient of the displacement field, the volumetric strain for each sub-volume ($\varepsilon_{v,i,n}$) could be computed to first-order by,

$$\varepsilon_{v,i,n} = tr(\varepsilon_{ij}) = \varepsilon_{xx,i,n} + \varepsilon_{yy,i,n} + \varepsilon_{zz,i,n} \tag{3}$$

Figure S3-c shows DVC-derived values for mean volumetric strain ($\bar{\varepsilon}_{v,n} = \sum_{i=1}^{k} \varepsilon_{v,i,n}$) plotted alongside the experimental values (Equation 3). At all values of l_s (excluding $l_s = 76$) the trend in DVC-derived values corresponded to the experimental trend, but underestimated the magnitude by 5-32%. For an edge length of 104 voxels, the underestimation was consistently ~13.5%, attributable to both the aforementioned error resulting from volume averaging and the influence of neglecting sub-volumes overlapping the tube wall. Whilst the absolute magnitudes of displacement and volumetric strain deviated slightly from experimental values, the character, trend and direction of soil displacements validate the measurement of displacement and volumetric strain for soil displacement velocities at the order of the root tip growth velocity (~800 $\mu m.h^{-1}$).

3.3. Root growth

The evolution in root extension rate (E) and rate of angular change in direction ($\Delta\theta$) are shown in Figure 5. The extension rate decreased gradually over the 20 h imaging period, with the mean extension rate ($\bar{E}$) being $800 \pm 75\ \mu\mathrm{m.h}^{-1}$. The angular change rate ($\Delta\theta$) peaked at 0.81 $rad.h^{-1}$ (at 9 h), falling back to a baseline value of ~0.3 $rad.h^{-1}$ for the remainder of the experiment. The mean rate of angular change ($\overline{\Delta\theta}$) was $0.28 \pm 0.09\ \mathrm{rad.h}^{-1}$.

3.4. Soil deformation at the root tip

3.4.1. Deformation projections

Figure 6 shows 2D deformation projections for each time-step, evidencing that isolated zones of deformation occurred far from the primary deformation zone. The raw data (Supplementary Video V1) suggest that these relate to fluid imbibition/draining events in macro-pore spaces. Figure 7 suggests that these fluid redistribution phenomena are not necessarily correlated with matrix deformation.

3.4.2. Digital volume correlation

Figure 8 shows full-field displacement data for all time-steps. At each time step, the morphology of the deformation zone is seen to correspond with the morphology observed in the respective 2D deformation projection (Figure 6). Displacements fell to undetectable levels well before the boundary of the field of view (FOV), indicating that assay size was adequate for the growth conditions. Over certain steps (i.e. 5 h, 6 h, 18 h), the maximum magnitude of the displacement field was ahead of the root tip, and over others (i.e. 2 h, 8 h, 17 h) was basal to the root tip. At the root tip, displacement vectors were predominantly oriented normal to the root surface, whereas >5mm behind the tip displacement orientations were predominantly parallel to the root surface.

Figure 5 shows global results. Plots of maximum and mean displacements evidenced the same oscillatory trend, differing only in amplitude, such that the steps of greatest local displacement were also the steps of greatest global displacement. The volumetric strain measured at each growth step gradually decreased over the course of the experiment, correlating with a gradual reduction in the root growth rate. The weighted mean of the angles between soil displacement vectors did not remain constant, but changed considerably over the experiment.

The mean correlation coefficient for the growth experiment was very high (0.994), and the minimum value (0.787) coincided with the step of maximum soil displacement (6 h).

4. Discussion

For the first time, *in vivo* XCT has allowed quantification of full-field soil deformation behaviour around a growing root tip. Across all time-steps, the displacement vectors in the immediate vicinity of the root tip were oriented approximately normal to the root surface, consistent with the morphologies of 2D displacement fields previously quantified around spherical penetrometers (Dexter and Tanner, 1972) and roots (Vollsnes et al., 2010) using DIC. This observation agrees with the proposal that the expanding meristem exerts pressure on the soil, redistributing the matrix to generate a cavity that accommodates the new root volume (Bengough and Mullins, 1990). The sub-volume size required at the root tip had an edge length of 3.01 mm, relative to the ~8 mm extent of the primary deformation zone from the root surface, providing acceptable sampling of the deformation region. However, it was not possible to infer from the DVC results the motion of discrete particles. For discrete particle tracking as opposed to quantification of continuum matrix deformation, a parallel family of approaches must be used (Hall et al., 2010).

In the more basal region of the root, displacements were normal to the root axis. This suggests that the velocities of any radial displacement components were too low relative to the sampling frequency to be quantified, given the thresholds of significance determined in the noise study.

The root followed a curved path during the experiment, and as observed by (Vollsnes et al., 2010), the magnitude of soil displacement was generally larger on the convex side of the root (Figure 8).

In all steps it was observed that by ~20 mm behind the root tip, the soil displacements had fallen below the threshold of significance. It is probable that deformation still occurs in this basal zone, but that the displacement per time-step is below the quantifiable threshold. It may also be that the spatial scale of these deformations is small relative to the sub-volume size, such that the values become vanishingly small due to the volume averaging inherent to DVC (Figure 9). Thus, to capture these lower velocity displacements, a slower scan frequency and/or smaller sub-volume size would be required, both of which would detrimentally impact the tracking of higher velocity deformations around the root tip. It is thus important in designing future studies that the time-step be matched to the velocity of the deformation of interest. Higher frequency imaging reduces the inter-scan displacement magnitude, and allows the use of smaller sub-volumes for a given displacement velocity, but increases the required number of correlations and thus the computational load. Given that the analysis per correlation takes of the order of hours on a workstation with 32 cores and 192 GB of RAM, the justification for increased sampling frequency must be carefully considered.

The single biological replicate considered here provides little scope for discussion of biophysical phenomena, but substantial heterogeneity in soil displacement magnitude and direction over time was evident. Soil physical factors that limit root growth rate vary with time and spatial location in the soil domain (Bengough et al., 2006), and roots are known to preferentially follow both paths of low penetration resistance in general (Sands et al., 1979) and macro-pore pathways in particular (Passioura, 1991). At the scale of root tip extension per step (~ 800 μm), the soil matrix was evidently highly heterogenous (Figure 7). Given the moderate inverse relationship observed between the soil displacement and root tip extension rate (Figure 5) we hypothesise that variable penetration resistance ahead of the root tip may be responsible for the variability in global soil deformation magnitude over time. Where a root tip can extend into existing macropores instead of displacing material to form a cavity, the resistance to extension will be reduced, and less soil displacement will be required per unit of root extension.

There are important factors of root/soil interaction that were not directly observable in these data, including mucilage exudation (Czarnes et al., 2000; McCully, 1999), and root hair traits (Moreno-Espíndola et al., 2007). Applying the techniques developed in this paper to investigate genotypes that contrast in mucilage exudation (Vollsnes et al., 2010) and root hair traits (Gahoonia et al., 2001) will offer compelling opportunities to probe the fundamentals of rhizosphere development.

5. Conclusion

This study has established a platform for explicit and quantitative *in vivo* analysis of soil deformation around growing roots. There is no particular constraint to the plant and soil material or growth conditions that can be investigated. The DVC parameters must be rigorously determined for each set of sample and imaging parameters, but this procedure is now standardised and provides a reliable measure of confidence in the results.

6. Acknowledgements

The authors thank the staff of the μVIS Centre for Computed Tomography for their assistance with imaging, and Prof. Fabrice Pierron for his technical suggestions which improved the manuscript. SDK has received funding under the EPSRC Doctoral Prize Scheme. SDK and TR have received funding from European Research Council consolidator grant 646809. NS was funded by an internship from the Faculty of Engineering and the Environment, University of Southampton.

7. Conflict of interest statement

The authors certify that they have no conflict of interest relating to financial concerns (such as honoraria; educational grants; participation in speakers' bureaus; membership, employment, consultancies, stock ownership, or other equity interest; and expert testimony or patent-licensing arrangements), or non-financial concerns (such as personal or professional relationships, affiliations, knowledge or beliefs) relating to this manuscript.

8. References

Ahrens, J., Geveci, B., Law, C., 2005. Paraview: An end user tool for large data visualization. Vis. Handbook. Ed. by CD Hansen CR Johnson. Elsevier.

Barré, P., Hallett, P.D., 2009. Rheological stabilization of wet soils by model root and fungal exudates depends on clay mineralogy. Eur. J. Soil Sci. 60, 525–538.

Bay, B.K., 2008. Methods and applications of digital volume correlation. J. Strain Anal. Eng. Des. 43, 745–760.

Bengough, A.G., Bransby, M.F., Hans, J., McKenna, S.J., Roberts, T.J., Valentine, T.A., 2006. Root responses to soil physical conditions; growth dynamics from field to cell. J. Exp. Bot. 57, 437–447.

Bengough, A.G., McKenzie, B.M., Hallett, P.D., Valentine, T.A., 2011. Root elongation, water stress, and mechanical impedance: a review of limiting stresses and beneficial root tip traits. J. Exp. Bot. 62 , 59–68. doi:10.1093/jxb/erq350

Bengough, A.G., Mullins, C.E., 1990. Mechanical impedance to root growth: a review of experimental techniques and root growth responses. J. soil Sci. 41, 341–358.

Cignoni, P., Corsini, M., Ranzuglia, G., 2008. Meshlab: an open-source 3d mesh processing system. Ercim news 73, 45–46.

Czarnes, S., Hallett, P.D., Bengough, A.G., Young, I.M., 2000. Root-and microbial-derived mucilages affect soil structure and water transport. Eur. J. Soil Sci. 51, 435–443.

Dexter, A.R., Tanner, D.W., 1972. Soil deformations induced by a moving cutting blade, an expanding tube and a penetrating sphere. J. Agric. Eng. Res. 17, 371–375.

Doube, M., Kłosowski, M.M., Arganda-Carreras, I., Cordelières, F.P., Dougherty, R.P., Jackson, J.S., Schmid, B., Hutchinson, J.R., Shefelbine, S.J., 2010. BoneJ: Free and extensible bone image analysis in ImageJ. Bone 47, 1076–1079.

Gahoonia, T.S., Nielsen, N.E., Joshi, P.A., Jahoor, A., 2001. A root hairless barley mutant for elucidating genetic of root hairs and phosphorus uptake. Plant Soil 235, 211–219.

Gillard, F., Boardman, R., Mavrogordato, M., Hollis, D., Sinclair, I., Pierron, F., Browne, M., 2014. The application of digital volume correlation (DVC) to study the microstructural behaviour of trabecular bone during compression. J. Mech. Behav. Biomed. Mater. 29, 480–499.

Gregory, P.J., Hutchison, D.J., Read, D.B., Jenneson, P.M., Gilboy, W.B., Morton, E.J., 2003. Non-invasive imaging of roots with high-resolution X-ray micro-tomography. Plant Soil 255, 351–359.

Hall, S.A., Bornert, M., Desrues, J., Pannier, Y., Lenoir, N., Viggiani, G., Bésuelle, P., 2010. Discrete and continuum analysis of localised deformation in sand using X-ray μCT and volumetric digital image correlation. Geotechnique 60, 315–322.

Jenneson, P.M., Gilboy, W.B., Morton, E.J., Gregory, P.J., 2003. An X-ray micro-tomography system optimised for the low-dose study of living organisms. Appl. Radiat. Isot. 58, 177–181.

Liu, L., Morgan, E.F., 2007. Accuracy and precision of digital volume correlation in quantifying displacements and strains in trabecular bone. J. Biomech. 40, 3516–3520. doi:10.1016/j.jbiomech.2007.04.019

McCully, M., 1999. ROOTS IN SOIL, Unearthing the Complexities of Roots and their Rhizospheres. Annu. Rev. Plant Physiol. Plant Mol. Biol. 50, 695–718.

Moreno-Espíndola, I.P., Rivera-Becerril, F., de Jesús Ferrara-Guerrero, M., De León-González, F., 2007. Role of root-hairs and hyphae in adhesion of sand particles. Soil Biol. Biochem. 39, 2520–2526.

Passioura, J.B., 1991. Soil structure and plant growth. Soil Res. 29, 717–728.

Perret, J.S., Al-Belushi, M.E., Deadman, M., 2007. Non-destructive visualisation and quantification of roots using computed tomography. Soil Biol. Biochem. 39, 391–399.

Peth, S., Nellesen, J., Fischer, G., Horn, R., 2010. Non-invasive 3D analysis of local soil deformation under mechanical and hydraulic stresses by μCT and digital image correlation. Soil Tillage Res. 111, 3–18.

Pierret, A., Kirby, M., Moran, C., 2003. Simultaneous X-ray imaging of plant root growth and water uptake in thin-slab systems. Plant Soil 255, 361–373. doi:10.1023/A:1026130532683

Sands, R., Greacen, E.L., Gerard, C.J., 1979. Compaction of sandy soils in radiata pine forests. I. A penetrometer study. Soil Res. 17, 101–113.

Schindelin, J., Arganda-Carreras, I., Frise, E., Kaynig, V., Longair, M., Pietzsch, T., Preibisch, S., Rueden, C., Saalfeld, S., Schmid, B., 2012. Fiji: an open-source platform for biological-image analysis. Nat. Methods 9, 676–682.

Schlüter, S., Leuther, F., Vogler, S., Vogel, H.J., 2016. X-ray microtomography analysis of soil structure deformation caused by centrifugation. Solid Earth 7, 129.

Tracy, S., Black, C., Roberts, J., McNeill, A., Davidson, R., Tester, M., Samec, M., Korošak, D., Sturrock, C., Mooney, S., 2012. Quantifying the effect of soil compaction on three varieties of wheat (<i>Triticum aestivum</i> L<i>.</i>) using X-ray Micro Computed Tomography (CT). Plant Soil 353, 195–208.

Vollsnes, A. V., Futsaether, C.M., Bengough, A.G., 2010. Quantifying rhizosphere particle movement around mutant maize roots using time-lapse imaging and particle image velocimetry. Eur. J. Soil Sci. 61, 926–939. doi:10.1111/j.1365-2389.2010.01297.x

Whalley, W.R., Leeds-Harrison, P.B., Clark, L.J., Gowing, D.J.G., 2005. Use of effective stress to predict the penetrometer resistance of unsaturated agricultural soils. Soil Tillage Res. 84, 18–27. doi:10.1016/j.still.2004.08.003

White, D.J., Take, W.A., Bolton, M.D., 2003. Soil deformation measurement using particle image velocimetry (PIV) and photogrammetry. Geotechnique 53, 619–631.

White, R.G., Kirkegaard, J.A., 2010. The distribution and abundance of wheat roots in a dense, structured subsoil--implications for water uptake. Plant. Cell Environ. 33, 133–148. doi:10.1111/j.1365-3040.2009.02059.x

Young, I.M., Crawford, J.W., 2004. Interactions and self-organization in the soil-microbe complex. Science 304, 1634–1637. doi:10.1126/science.1097394

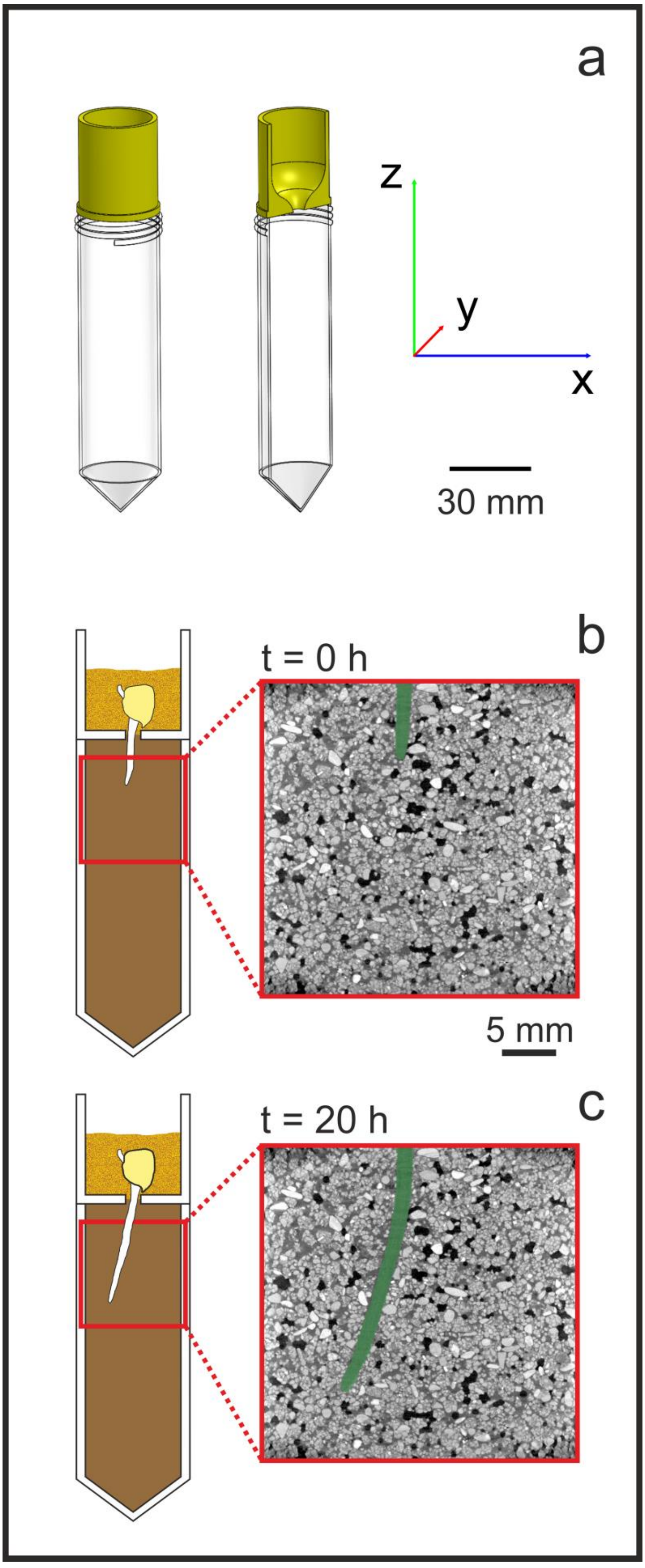

a
z
y
x
30 mm
b
t = 0 h
5 mm
c
t = 20 h

Figure 1 –Schematic of the growth assay (a). The root was imaged over a period of 20 h. The *xz* planar sections through the XCT data show the initial (b) and final (b) extent of growth at 0 h and 18 h respectively.

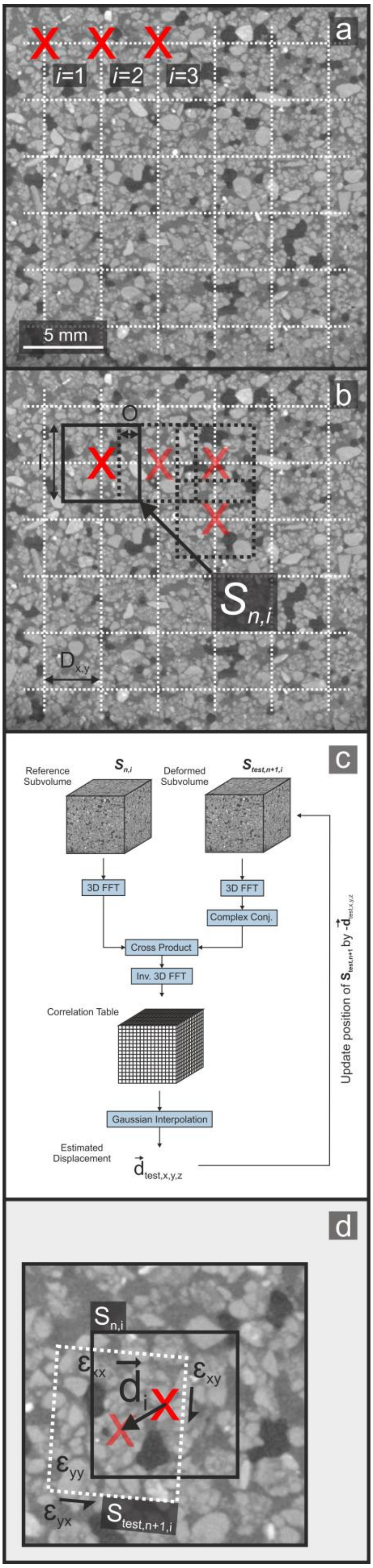

a
i=1
i=2
i=3
5 mm
b
O
l
S n,i
D x,y
c
Reference Subvolume
S n,i
Deformed Subvolume
S test,n+1,i
3D FFT
3D FFT
Complex Conj.
Cross Product
Inv. 3D FFT
Correlation Table
Gaussian Interpolation
Estimated Displacement
d test,x,y,z
Update position of S test,n+1 by -d test,x,y,z
d
S n,i
ε xx
d i
ε xy
ε yy
ε yx
S test,n+1,i

Figure 2 - A simplified schematic of the correlation algorithm. (a) An initial image (image n) taken at $t = t_1$ is divided into a grid. (b) At each i of k intersections, a sub-region ($S_{1,i,n}$) is defined, having isotropic edge length l. The ratio of centroid spacing ($D_{x,y}$) to edge length $\{l\}$ defines the overlap $\{o\}$. Crosses mark the sub-region centroids. (c) Each sub-region from image n ($S_{n,i}$) is compared with a sub-region centred on the same location in the deformed image ($S_{test,n+1,i}$) acquired at $t = t_2$. The process flow for a single iteration of the FFT algorithm is shown. The estimate for each pass updates the position of $S_{test,n+1,i}$. (d) When displacements have been estimated for all k sub-regions in the domain, the strain tensor for each sub-volume is determined from the gradient of the displacement field.

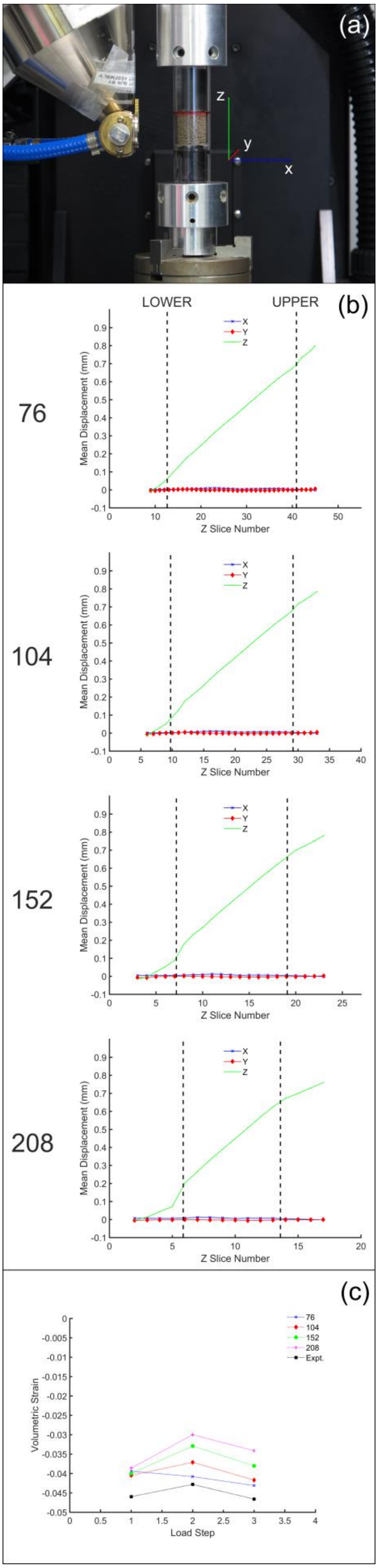
(a)
z
y
x
(b)
LOWER
UPPER
76
104
152
208
X
Y
Z
Mean Displacement (mm)
Z Slice Number
(c)
76
104
152
208
Expt.
Volumetric Strain
Load Step

Figure 3 - (a) The uniaxial compression rig used for soil compression tests, shown mounted in the Nikon HMX 225 XCT scanner. (b) With an upper-platen displacement of 0.8 mm applied, the mean of the DVC-derived displacement, volumetric strain and shear strain over the gauge length are shown for sub-volume sizes of 76, 104, 152 and 208 voxels. The position of upper and lower platens is indicated in each case by dashed lines. (c) The sequential volumetric strains over three iterations of platen displacement, computed using DVC at different sub-volume sizes, and separately validated (black line) using the change in gauge volume.

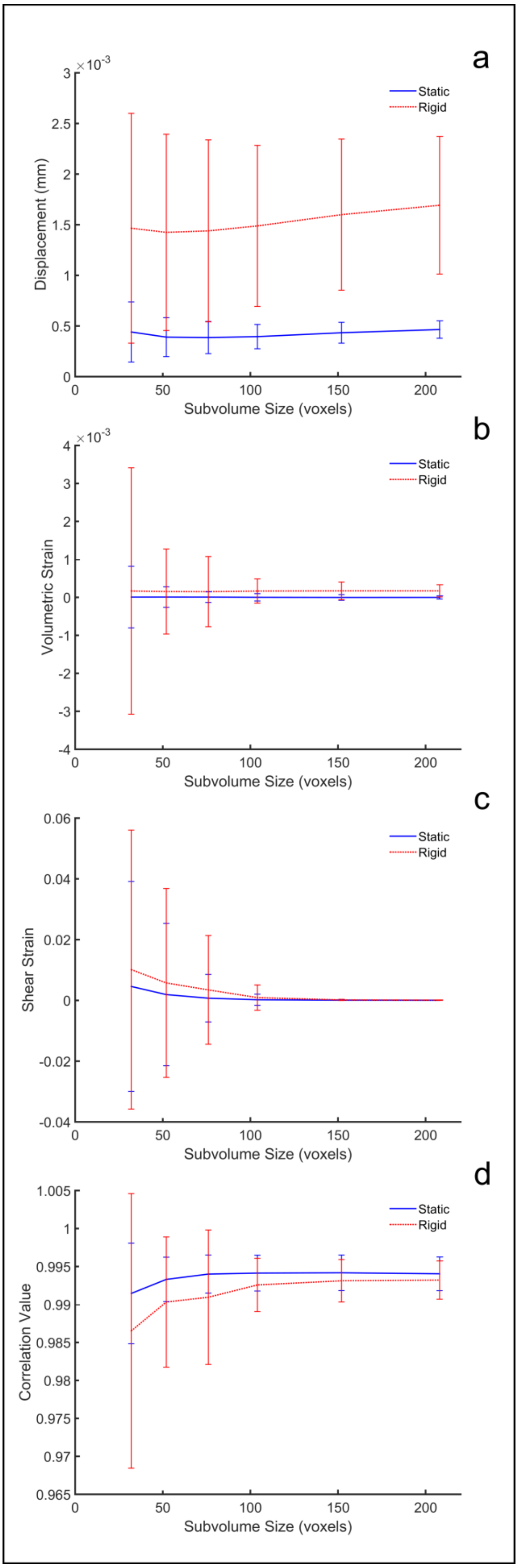

a
Displacement (mm)
×10^-3
Static
Rigid
Subvolume Size (voxels)
b
Volumetric Strain
×10^-3
Static
Rigid
Subvolume Size (voxels)
c
Shear Strain
Static
Rigid
Subvolume Size (voxels)
d
Correlation Value
Static
Rigid
Subvolume Size (voxels)

Figure 4 - The results of the noise calibration study to determine the optimal sub-volume edge length. Plots of DVC result versus sub-volume edge length are shown for (a) mean displacement, (b) mean volumetric strain, (c) mean shear strain, and (d) mean correlation value. The optimal sub-volume edge length was 104 voxels, based on convergence of offset (deviation from zero) and noise (standard deviation, indicated by error bars).

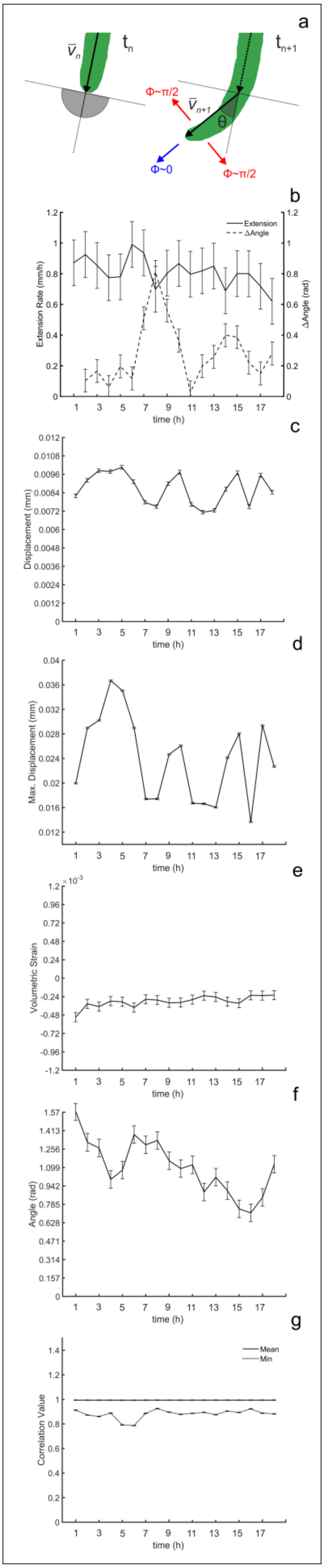
a
$\bar{v}_n$
t_n
t_{n+1}
Φ~π/2
$\bar{v}_{n+1}$
θ
Φ~0
Φ~π/2
b
Extension
ΔAngle
Extension Rate (mm/h)
ΔAngle (rad)
time (h)
c
Displacement (mm)
time (h)
d
Max. Displacement (mm)
time (h)
e
Volumetric Strain
time (h)
f
Angle (rad)
time (h)
g
Mean
Min
Correlation Value
time (h)

Figure 5 – (a) The growth direction of the root over the period $\Delta t = t_n - t_{n-1}$ is approximated by vector $\vec{v}_n$. The extension rate is given by the vector modulus ($|\vec{v}_n|$) between scans. The angle θ denotes the change in heading between successive growth vectors (Equation 1). The angle φ denotes the magnitude-weighted mean angle between soil displacement vectors and the direction of root growth (Equation 4). Plots show the bulk results for: (b) extension rate and rate of change in growth direction (θ); (c) mean soil displacement; (d) maximum soil displacement; (e) volumetric strain; (f) the magnitude-weighted mean of angles between displacements and the root growth vector (φ); (g) the mean and minimum correlation coefficients.

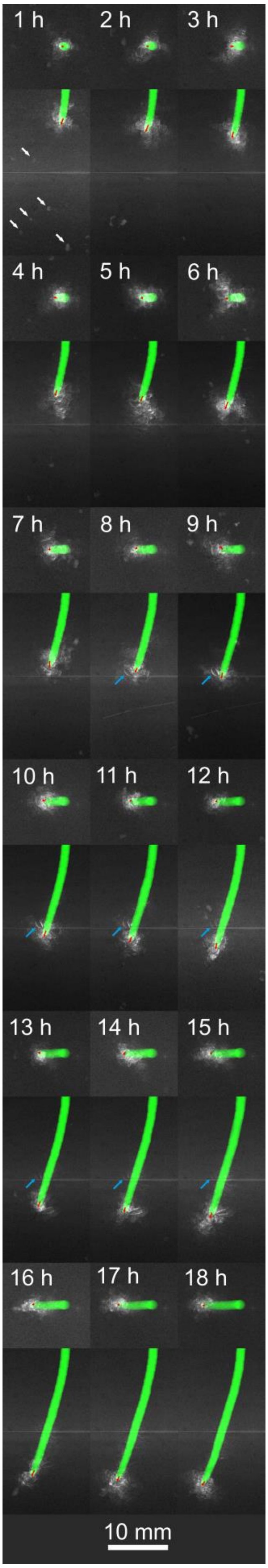
1 h
2 h
3 h
4 h
5 h
6 h
7 h
8 h
9 h
10 h
11 h
12 h
13 h
14 h
15 h
16 h
17 h
18 h
10 mm

Figure 6 - Images of the deformation field generated by subtraction of sequential volumes from one another and projection of the resulting difference volumes along z and y axes (Equation 2). The time step is indicated in each case, and the red vector indicates the Euclidian approximation of growth ($\vec{v}_n$) between the current and previous images. Some streaking artifacts are evident. The morphology of the deformation zone changes between growth steps. The deformation zone is sometimes predominantly lateral to the root tip (i.e. 10 h, 15 h) and sometimes predominantly beneath the tip (i.e. 5 h, 6 h, 16 h, 17 h). The arrows at 1 h indicate pore draining/filling events (see Figure 5) in the region away from the primary deformation zone at the root tip.

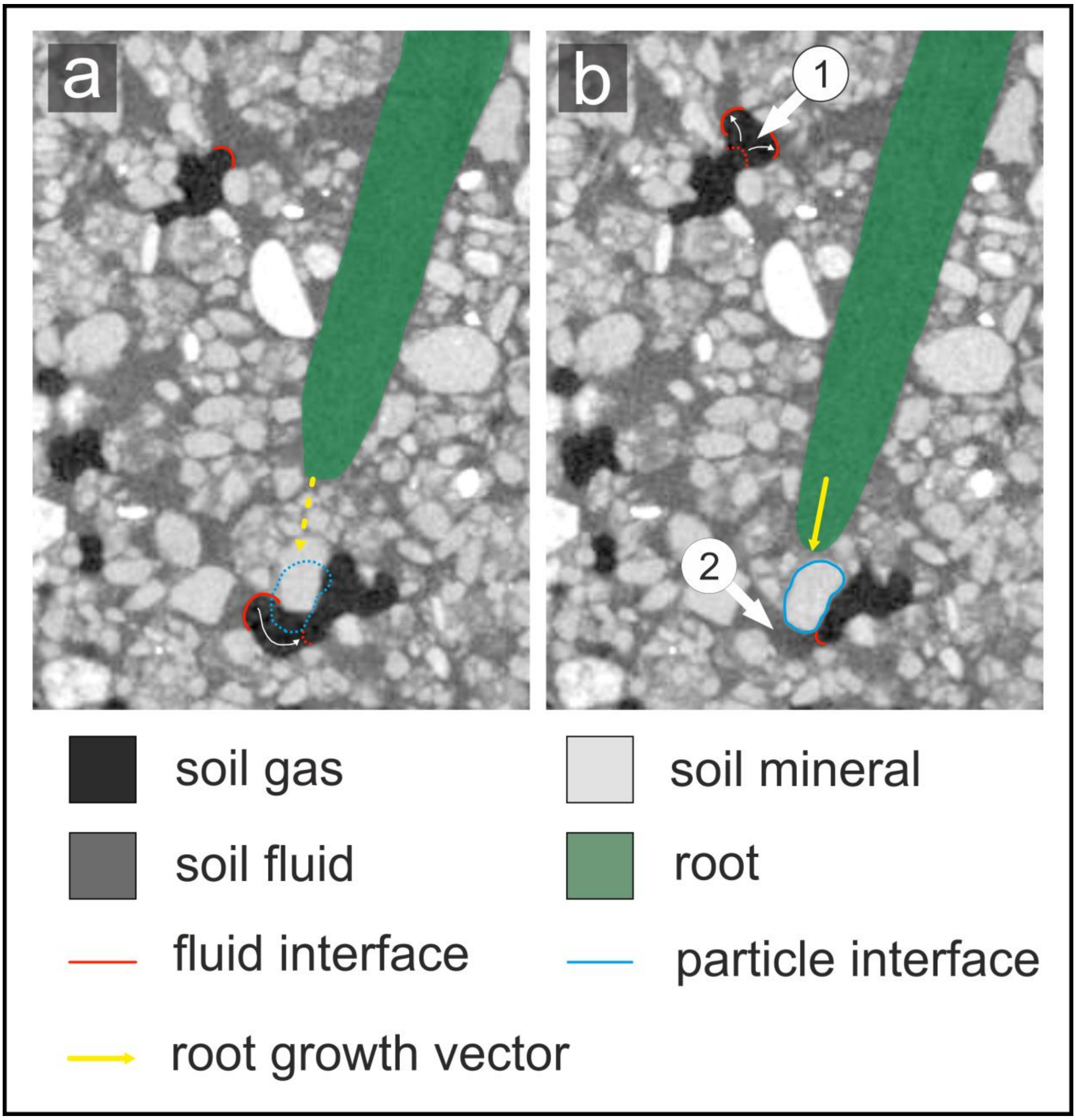

Figure 7 –Deformation behaviour is shown qualitatively for a 2D section of XCT data, over a single growth step (11 h – 12 h). Over the 1 h interval between (a) and (b), the root tip extended along vector $\vec{v}_n$ approximated by the yellow arrow, and the fluid/gas interfaces at locations (1) and (2) moved. At location (1), this interface movement (i.e. Haines jump) occurred without obvious soil matrix deformation in the pore region. At location (2), the interface movement coincided with obvious rigid-body movement of a soil grain driven by the extension of the root tip, resulting in a macro-pore volume change.

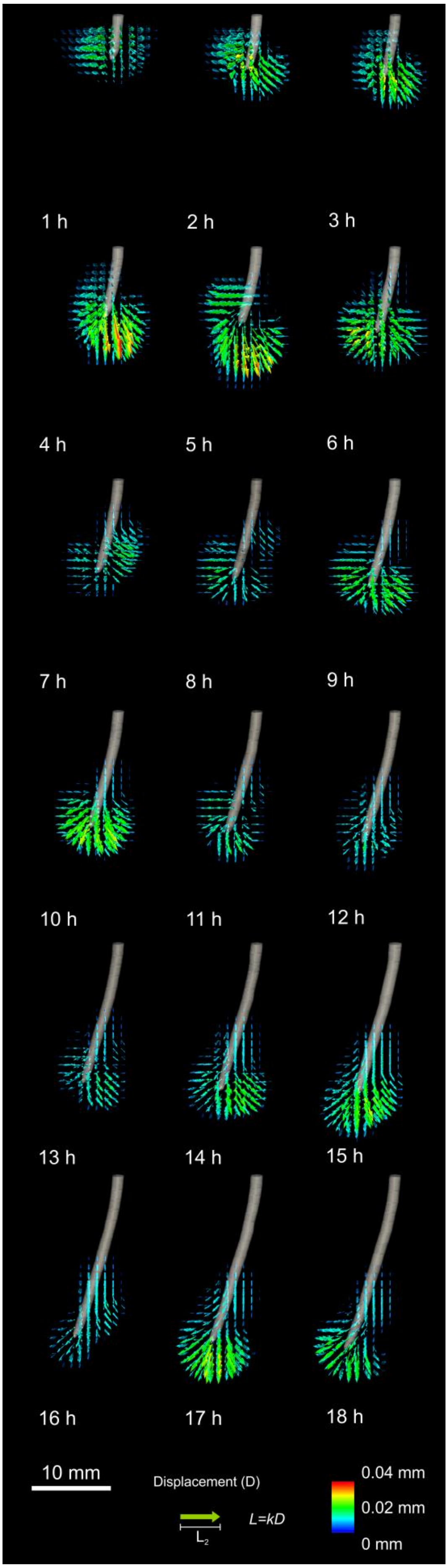
1 h
2 h
3 h
4 h
5 h
6 h
7 h
8 h
9 h
10 h
11 h
12 h
13 h
14 h
15 h
16 h
17 h
18 h
10 mm
Displacement (D)
L=kD
L2
0.04 mm
0.02 mm
0 mm

Figure 8 - The full-field displacement fields generated using the FFT DVC algorithm. The time step is indicated in each case. Each displayed vector length (L) has been scaled from the actual displacement magnitude (D) by a factor k for easier visualisation. The colour-map indicates the actual vector magnitude (D).

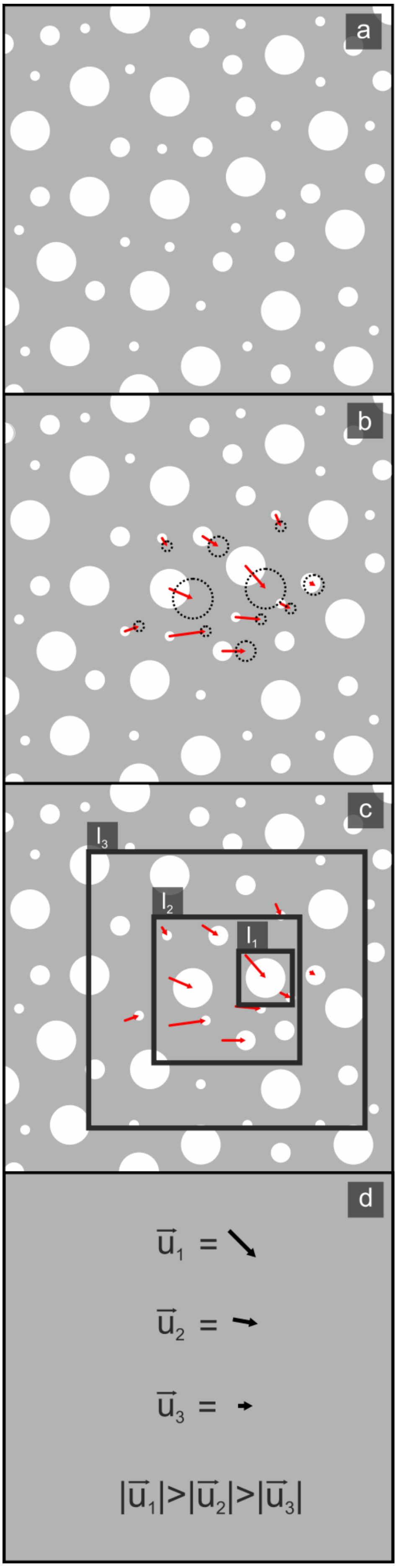
a
b
c
l_3
l_2
l_1
d
$\vec{u}_1 =$
$\vec{u}_2 =$
$\vec{u}_3 =$
$|\vec{u}_1|>|\vec{u}_2|>|\vec{u}_3|$

Figure 9 - The magnitude and spatial resolution of the DVC results are a function of sub-region size. This is shown schematically for a granular material (a) in which a localised deformation of grains has occurred (b). Assuming high correlation coefficients are attainable in all cases, a sub-region edge length at the single-particle length scale (I_1) will result in a magnitude and direction of displacement at the scale of discrete particle motion (c). If the edge length is increased to include a larger number of particles (I_2), the usual prerequisite for adequate correlation coefficient, the displacement represents the average of particle movement within the region. If the sub-region size becomes large relative to the scale of the local deformation zone (I_3), the estimated displacement will be decreased relative to the maximum particle motion, since a greater proportion of the enclosed region is static. Thus the greater the sub-volume size, the more the sub-volume displacement may differ in direction and magnitude to the displacement of the grain of maximum displacement within the sub-volume.

System	Nikon HMX225 ST
Mode	Static reflecting target
Target material	Tungsten
Detector size	2048x2048
Projections	1571
Frames per projection	4
Voltage (kV)	180
Current (μA)	65
Exposure (ms)	67
Binning	2x2
Filtering	None
Shuttling	None
Voxel edge length (μm)	29.8
Source to sample (mm)	30

Table 1 – X-Ray CT imaging parameters.